



Cite this: *Nanoscale Adv.*, 2020, **2**, 4785

## Boosting the performance of $\text{NO}_2$ gas sensors based on n–n type mesoporous $\text{ZnO}@\text{In}_2\text{O}_3$ heterojunction nanowires: *in situ* conducting probe atomic force microscopic elucidation of room temperature local electron transport†

Ramakrishnan Vishnuraj, Karthikeyan K. Karuppanan, Mahaboobbatcha Aleem and Biji Pullithadathil  \*

Herein, n–n type one dimensional  $\text{ZnO}@\text{In}_2\text{O}_3$  heterojunction nanowires have been developed and their local electron transport properties during trace-level  $\text{NO}_2$  gas sensing process have been probed at room-temperature using conducting probe atomic microscopy. Solvothermally synthesized 1D  $\text{ZnO}@\text{In}_2\text{O}_3$  heterojunction nanowires have been characterized by various spectroscopic and microscopic techniques, which revealed the mesoporous structure indicating their enhanced sensing properties. The dangling bonds and fraction of metal ions to oxygen ions existing on the exposed crystal facets of the heterojunction nanowires have been visualized by employing crystallographic simulations with TEM analysis, which aided in forecasting the nature of surface adsorption of  $\text{NO}_2$  gas species. *In situ* electrical characteristics and Scanning Spreading Resistance Microscopic (SSRM) imaging of single  $\text{ZnO}@\text{In}_2\text{O}_3$  heterojunction nanowires revealed the local charge transport properties in n–n type  $\text{ZnO}@\text{In}_2\text{O}_3$  heterojunction nanowires. Moreover, the  $\text{ZnO}@\text{In}_2\text{O}_3$  heterojunction nanowires based sensor exhibited excellent sensitivity ( $S = 274\%$ ), a fast response (4–6 s) and high selectivity towards trace-level concentration (500 ppb) of  $\text{NO}_2$  gas under ambient conditions with low power consumption. Spatially resolved surface potential (SP) variations in  $\text{ZnO}@\text{In}_2\text{O}_3$  heterojunction nanowires have been visualized using *in situ* Scanning Kelvin Probe Force Microscopy (SKPM) under  $\text{NO}_2$  gas environment at room temperature, which was further correlated with its energy band structure. The work functions of the material evaluated by SKPM reveal considerable changes in the energy band structure owing to the local electron transport between  $\text{ZnO}$  and  $\text{In}_2\text{O}_3$  at the heterojunctions upon exposure to  $\text{NO}_2$  gas indicating the charge carrier recombination. A plausible mechanism has been proposed based on the experimental evidences. The results suggest that new insights into complex sensing mechanisms deduced from the present investigation on n–n type MOS based heterojunction nanowires under ambient conditions can pave the way for the novel design and development of affordable and superior real-time gas sensors.

Received 23rd April 2020  
Accepted 10th August 2020

DOI: 10.1039/d0na00318b  
[rsc.li/nanoscale-advances](http://rsc.li/nanoscale-advances)

## Introduction

Among various environmental pollutants released from industrial and automobile emissions,  $\text{NO}_2$  is considered as the most dangerous air pollutant, as it leads to serious health hazards, and plays a major role in depletion of ozone ( $\text{O}_3$ ) and acid rains.<sup>1</sup> Hence, it is highly essential to detect trace level  $\text{NO}_2$  gas for environmental monitoring, human health and safety.<sup>2</sup> To address these serious concerns, incredible attempts have been

focused on advancement of  $\text{NO}_2$  gas sensors based on metal-oxide semiconductors (MOSSs).  $\text{ZnO}$ ,<sup>3</sup>  $\text{Co}_3\text{O}_4$ ,<sup>4</sup>  $\text{SnO}_2$ ,<sup>5</sup>  $\text{WO}_3$ ,<sup>6</sup>  $\text{NiO}$ ,<sup>7</sup>  $\text{In}_2\text{O}_3$ ,<sup>8</sup> etc. have attracted tremendous interest in the gas sensor sector owing to their inexpensiveness, simple fabrication and superior sensing performance. Among various MOS materials,  $\text{ZnO}$  and  $\text{In}_2\text{O}_3$  possess wider band gaps and have been realized for variety of applications, including gas sensors, solar cells,<sup>9</sup> transparent conducting oxides<sup>10</sup> etc.  $\text{ZnO}$  having a hexagonal crystal plane arrangement with a wurtzite structure along with a huge exciton binding energy of 60 meV is considered to be an ideal semiconductor for  $\text{NO}_2$  gas sensors.<sup>11–13</sup> However, though  $\text{ZnO}$  is being used in conventional MOS gas sensors, the issues associated with poor selectivity, high operating temperature and reliability hinder its practical applications. Similarly,

Nanosensor Laboratory, PSG Institute of Advanced Studies, Coimbatore-641 004, India. E-mail: bijuja123@yahoo.co.in; pbm@psgias.ac.in

† Electronic supplementary information (ESI) available. See DOI: [10.1039/d0na00318b](https://doi.org/10.1039/d0na00318b)



n-type  $\text{In}_2\text{O}_3$  (rhombohedral structure) has also gained significant attention towards  $\text{NO}_2$  detection owing to its unique characteristics such as an extensive energy gap (2.5–3.75 eV), high electrical conductivity *etc.*<sup>14</sup> However, pristine  $\text{ZnO}$  and  $\text{In}_2\text{O}_3$  based sensors have found limited practical applicability due to their adverse effects in selectivity, higher operating temperature and poor response at trace level gas concentrations. Numerous studies have attempted to improve their sensing properties by modification with noble metals, surface alteration and shaping with p-n or n-n heterojunctions with alternate MOSSs. Mostly, binary oxide heterojunctions formed at the interfaces found to play an important role in augmenting sensing properties. The formation of n-n heterojunctions induces synergistic effects due to coupling of binary oxides with a minimal difference in work functions. Until now, n-n type binary oxide MOS nanohybrids, such as  $\text{ZnO/SnO}_2$ ,<sup>15</sup>  $\text{WO}_3/\text{ZnO}$ ,<sup>16</sup>  $\text{WO}_3/\text{In}_2\text{O}_3$ ,<sup>17</sup>  $\text{TiO}_2/\text{ZnO}$ ,<sup>18</sup> *etc.* have shown the significance of hetero-interfaces towards detection of noxious  $\text{NO}_2$ . In this scenario, hierarchical hetero-nanostructures with a unique combination of  $\text{ZnO}$  and  $\text{In}_2\text{O}_3$  could be expected to exhibit excellent  $\text{NO}_2$  gas sensing properties with easy fabrication, long-term stability and enhanced sensitivity.<sup>3,19</sup> However, the design of such heterojunction MOS based gas sensors demands precise understanding of the complex sensing mechanism for suitably deploying them for real time applications. Although there are a number of existing reports describing the sensing mechanism of pristine MOSSs, there is a serious lack of systematic investigations on heterojunction metal oxide materials owing to their interfacial structural complexity. Based on the literature, it can be ascertained that the development of high aspect ratio, one-dimensional MOS heterojunction nanostructures can greatly influence the sensing properties such as the gas response, sensitivity and selectivity.<sup>20,21</sup> Advancements of n-n type MOS heterojunctions could be an appropriate strategy to extend the execution of gas sensors, but, comprehensive investigations pertaining to the complex sensing mechanisms are still under the infancy stage. Also, the crystallographic dependency of dissimilar heterojunction MOS materials on their gas sensor performance has not yet been thoroughly discussed.

Operando and *in situ* techniques, based on DRIFT,<sup>7,19</sup> Raman spectroscopy,<sup>22</sup> photoluminescence spectroscopy,<sup>23</sup> XPS,<sup>24,25</sup> UV-DRS,<sup>26</sup> EPR,<sup>27</sup> *etc.* have been utilized to elucidate the sensing mechanism of pristine MOSSs towards different gases. Recently, Patsha *et. al.*, reported local electron transfer process and surface band bending during methane sensing by pristine GaN nanowires using *in situ* SKPM analysis.<sup>28</sup> Kaur *et. al.*, attempted to explore the charge transfer mechanism of a polypyrrole–tin oxide nanocomposite (PPy– $\text{SnO}_2$ ) nanowire based  $\text{NH}_3$  sensor using *in situ* SKPM studies.<sup>29</sup> But, so far, no reports are available on exploration of complex sensing mechanism of MOS based heterojunction materials using *in situ*/operando studies.

Our previous report demonstrated the enhanced  $\text{NO}_2$  sensing and electron transport properties of n-p type ultra-long  $\text{ZnO@Bi}_2\text{O}_3$  heterojunction nanorods.<sup>32</sup> Though the ultra-long  $\text{ZnO}$  based n-p type  $\text{ZnO@Bi}_2\text{O}_3$  heterojunction nanorods showed superior  $\text{NO}_2$  sensing performances, the high operating temperature limited their possible practical applications. With

this investigation, we have developed n-n type  $\text{ZnO@In}_2\text{O}_3$  heterojunction nanowires, which can operate at reduced operating temperature with sustainable sensitivity. The surface activity of  $\text{ZnO}$  could be enhanced by coalescence of  $\text{In}_2\text{O}_3$  nanoislands on the surface that can act as a lever of charge transfer during exposure of  $\text{NO}_2$  gas and aided in the augmentation of sensing characteristics. So far, very few reports have attempted SKPM to demonstrate the sensing behaviour of nanomaterials.<sup>28–31</sup> To the best of our knowledge, this is the first report on room-temperature local charge transport properties for unravelling the complex mechanism pertaining to  $\text{NO}_2$  sensing properties of mesoporous n-n type  $\text{ZnO@In}_2\text{O}_3$  heterojunction nanowires based on SKPM and SSRM. The  $\text{NO}_2$  sensing properties of pristine  $\text{ZnO}$  nanowires and  $\text{ZnO@In}_2\text{O}_3$  heterojunction nanowires were investigated towards trace level  $\text{NO}_2$  gas, and  $\text{ZnO@In}_2\text{O}_3$  heterojunction nanowires exhibited excellent sensitivity, improved selectivity and rapid response and recovery time at room temperature, indicating their potential usage in real time applications.

## Experimental section

### Materials used

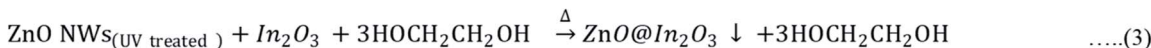
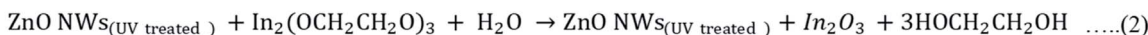
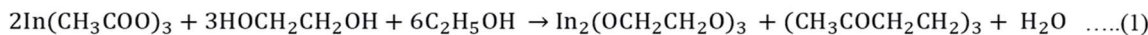
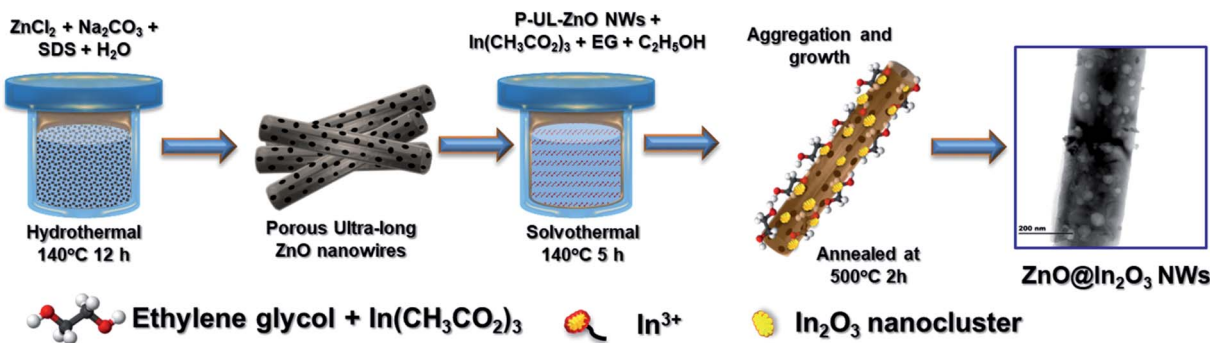
Zinc chloride dihydrate ( $\text{ZnCl}_2 \cdot 2\text{H}_2\text{O}$ , 99.8%, Merck), indium acetate ( $\text{In}(\text{CH}_3\text{COO})_3$ , 99.99%, Sigma Aldrich), sodium dodecylbenzene sulfonate (SDS, 99.97%, Merck), sodium carbonate ( $\text{Na}_2\text{CO}_3$ , 99.9%, Merck), ethylene glycol (EG, 99.8%, Merck), and ethanol ( $\text{C}_2\text{H}_5\text{OH}$ , 99%, Merck) were used without any further purification.

### Synthesis of porous $\text{ZnO@In}_2\text{O}_3$ heterojunction nanowires

Porous  $\text{ZnO}$  nanowires were chemically synthesized by simple hydrothermal method as per our previous reports.<sup>32,33</sup> In this investigation, n-n type  $\text{ZnO@In}_2\text{O}_3$  heterojunction nanowires were synthesized by solvothermal process. Briefly, 0.5 mM of  $\text{In}(\text{CH}_3\text{COO})_3 \cdot x\text{H}_2\text{O}$  was dissolved in a binary solvent consisting of 1 : 3 fraction of ethylene glycol and ethanol followed by 40 min of vigorous stirring. Meanwhile, the surface treatment of 200 mg of  $\text{ZnO}$  nanowires was carried out using UV-irradiation (254 nm) for 2 min. The above solution was ultrasonicated for 30 min in order to form a homogenous solution. Further, the solution was subjected to heat treatment at 160 °C for 4 h after shifting to a Teflon-sealed SS autoclave of 100 mL capacity. The resultant product was collected; washed and centrifuged several times with 80% ethanol and deionized water to remove the unwanted  $\text{In}_2\text{O}_3$  impurities. The product was dried overnight in a hot air oven at 90 °C. The ensuing amorphous precipitate was heat treated for 3 h at 550 °C in air at a ramp rate of 5 °C min<sup>-1</sup>. After the annealing process, the color of the product turned to light yellow, indicating the crystallization of  $\text{In}_2\text{O}_3$  nanoislands on the  $\text{ZnO}$  nanowires.

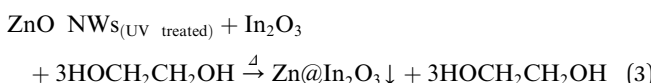
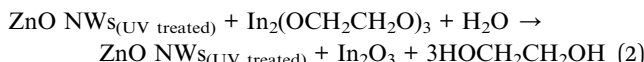
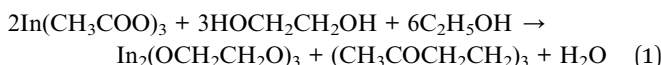
## Results and discussion

Mesoporous  $\text{ZnO}$  nanowires were chemically synthesized *via* a simple hydrothermal technique.<sup>34</sup> Scheme 1 illustrates the formation mechanism of  $\text{In}_2\text{O}_3$  nanoislands on  $\text{ZnO}$  nanowires



Scheme 1 Schematic diagram of the synthesis method adopted for n-n type  $\text{ZnO@In}_2\text{O}_3$  heterojunction nanowires.

formed *in situ* using  $\text{In}(\text{CH}_3\text{COO})_3$  as the precursor. The chemical reactions during the formation of heterojunction  $\text{ZnO@In}_2\text{O}_3$  nanowires can be represented as per eqn (1-3). The purified UV-irradiated  $\text{ZnO}$  nanowires possess more surface active sites and in the binary solvent of ethanol and ethylene glycol,  $\text{In}^{3+}$  gets effectively adsorbed over the surface of  $\text{ZnO}$  nanowires through hydrogen bonding. During the solvothermal hydrolysis process, the  $\text{In}_2\text{O}_3$  nanoislands were firmly anchored over the surface of  $\text{ZnO}$  nanowires by initially forming a relatively stable complex (indium ethylene glycolate) due to the strong coordination between indium ions and surface active functional groups of  $\text{ZnO}$  nanowires. The solvothermal process with the aid of pressure and temperature inevitably induces Ostwald ripening that causes the self-organization of  $\text{In}_2\text{O}_3$  nanoislands on the surface of  $\text{ZnO}$  nanowires.<sup>35</sup> The resultant mesoporous  $\text{ZnO@In}_2\text{O}_3$  heterojunction nanowires were found to be amorphous in nature. The material was further subjected to a high temperature (550 °C) annealing process under oxygen atmosphere in order to improve the crystallinity, and the white powder turned pale yellow.



### Structural and morphological characterization of mesoporous $\text{ZnO@In}_2\text{O}_3$ heterojunction nanowires

Fig. 1(a) shows the XRD patterns of thermal treated  $\text{ZnO}$  nanowires and  $\text{ZnO@In}_2\text{O}_3$  heterojunction nanowires. The

highly intense peaks observed at various diffraction angles ( $2\theta$ ) of 32.03°, 34.79°, 36.43°, 47.69°, 56.74°, 63.15°, 68.07° and 69.20° correspond to the crystal planes (100), (002), (101), (110), (103), (200), (112) and (201) of  $\text{ZnO}$ . The respective peaks matching the hexagonal wurtzite crystal structure of  $\text{ZnO}$  were indexed (JCPDS card no. 36-1451), with lattice parameters of  $a = 3.249 \text{ \AA}$  and  $c = 5.206 \text{ \AA}$ . The absence of additional peaks clearly confirms the purity of  $\text{ZnO}$  nanowires. The calculated fraction of intensity among the (101) and (100) planes ( $I_{100}/I_{101}$ ) of the  $\text{ZnO}$  nanowires was found to be higher than that of pristine  $\text{ZnO}$  which evidently reflected in the preferential growth of  $\text{ZnO}$  nanowires along the  $\langle 100 \rangle$  direction. In addition to the  $\text{ZnO}$  peaks (hexagonal wurtzite structure), the  $\text{ZnO@In}_2\text{O}_3$  nanowires also showed peaks at 22.33°, 30.97°, 32.59°, 45.57°, 52.41°, and 72.84° which are attributed to the lattice planes of (012), (104), (110), (024), (116) and (312) of the rhombohedral  $\text{In}_2\text{O}_3$  crystal structure (JCPDS no. #73-1809), suggesting the formation of heterojunctions.<sup>36</sup>

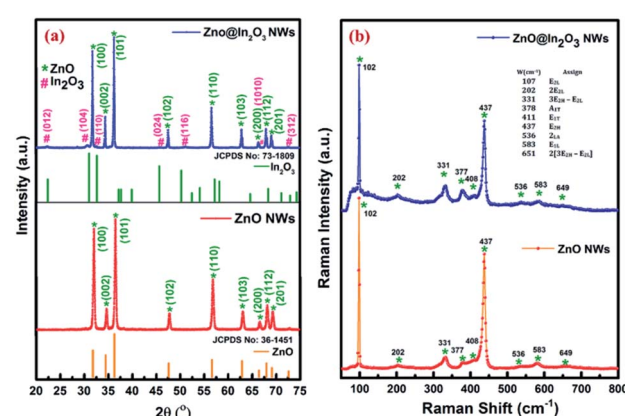


Fig. 1 (a) XRD patterns and (b) Raman spectra of  $\text{ZnO}$  nanowires and  $\text{ZnO@In}_2\text{O}_3$  heterojunction nanowires.



Fig. 1(b) presents the room-temperature Raman peak shifts observed for ZnO nanowires and ZnO@In<sub>2</sub>O<sub>3</sub> heterojunction nanowires using the excitation wavelength of a 532 nm laser source in the backscattering mode. The Raman spectral analysis of ZnO nanowires showed an intense peak at 438 cm<sup>-1</sup> confirming the hexagonal wurtzite structure, which corresponds to the E<sub>2</sub> high mode of ZnO. Furthermore, the peaks that appeared at the lower frequency range of 329 cm<sup>-1</sup> and 378 cm<sup>-1</sup> are related to the zone edging phonon vibrations, E<sub>2</sub> high – E<sub>2</sub> low and A<sub>1</sub>(TO), respectively.<sup>37</sup> A wide peak observed at 583 cm<sup>-1</sup> assigned to E<sub>1</sub>(LO) confirms the presence of more oxygen vacancies (V<sub>O</sub>) and zinc interstitials (Zn<sub>i</sub>). The considerable shifts noticed for the ZnO@In<sub>2</sub>O<sub>3</sub> heterojunction nanowires could be due to the charge transfer at the interfaces of In<sub>2</sub>O<sub>3</sub> nanoislands grown on the ZnO nanowires. The overall peak intensity was found to be suppressed due to the growth pattern of In<sub>2</sub>O<sub>3</sub> nanoislands formed over the ZnO nanowires. The peak related to the E<sub>1</sub> (LO) mode of ZnO was suppressed due to the presence of interstitial defects, which acted as favorable sites for the growth of In<sub>2</sub>O<sub>3</sub> nanoislands. The peak related to the E<sub>2</sub> (high) mode was found to be wide and weak, same as that observed in the amorphous phase, which might be due to the formation of heterojunctions between Zn–O and In–O bonds. The fading of the A<sub>1</sub>(LO) mode at 583 cm<sup>-1</sup> is because of the existence of zinc interstitials, oxygen vacancy states, etc.<sup>38</sup>

The HRTEM images of pristine porous ZnO nanowires and porous ZnO@In<sub>2</sub>O<sub>3</sub> heterojunction nanowires are shown in Fig. 2 and S2.<sup>†</sup> The In<sub>2</sub>O<sub>3</sub> nanoislands were found to be evenly anchored over the ZnO nanowires with a mean particle size of 12 ± 0.25 nm which confirmed the formation of ZnO–In<sub>2</sub>O<sub>3</sub> interfaces (Fig. 2(a)). HRTEM analysis of the hybrid nanowires revealed a well-resolved inter-planar spacing related to ZnO with  $d(002) = 2.67 \text{ \AA}$  and In<sub>2</sub>O<sub>3</sub> with  $d(110) = 2.73 \text{ \AA}$ . Though HRTEM of ZnO and In<sub>2</sub>O<sub>3</sub> indicated the exposed planes, such as (002) and (110) respectively, it should be noted that the interplanar distance between the (002) plane of ZnO and the (110) plane of In<sub>2</sub>O<sub>3</sub> was observed to be matching as depicted in Fig. 2(e–f). Accommodating the lattice strain at the heterojunctions, In<sub>2</sub>O<sub>3</sub> nanoislands exhibited an interplanar spacing of 2.91 Å corresponding to the (104) plane anchored on the surface of ZnO nanowires, as observed from Fig. 2(g). From the HRTEM analysis, it is evident that the (002) crystal plane of ZnO and the (110) plane of In<sub>2</sub>O<sub>3</sub> are highly exposed to the NO<sub>2</sub> molecules. Further, these facets were simulated via CaRIne crystallography 3.1 to visualize the dangling bonds existing in the respective planes and to estimate the proportions of Zn<sup>2+</sup> to O<sup>2-</sup> at the ZnO lattice and In<sup>3+</sup> to O<sup>2-</sup> at the In<sub>2</sub>O<sub>3</sub> lattice. The SAED pattern of ZnO@In<sub>2</sub>O<sub>3</sub> nanowires is shown in Fig. 2(d). The planes (100), (110), (203) and (002) represent the ZnO crystal lattice and the planes (211), (104), (208) and (104) correspond to the In<sub>2</sub>O<sub>3</sub> crystal lattice as deduced from the JCPDS card no. 36-1451 for ZnO with the hexagonal wurtzite structure and JCPDS card no. 73-1809 for In<sub>2</sub>O<sub>3</sub> with the rhombohedral structure.

These virtual crystal planes were simulated for visualizing the exposed facets along with the dangling bonds and correlated with HRTEM analysis. For the (002) lattice plane terminated with Zn<sup>2+</sup>, the chemisorption capability could be preferred since the

Zn<sup>2+</sup> ions existing on the (002) plane are able to seize more oxygen from the atmosphere which further responds towards NO<sub>2</sub> molecules through unsaturated oxygen coordination aided by physisorption processes.<sup>39</sup> Fig. 2(h) presents the simulated crystal plane after slicing the (002) facet of ZnO, the (104) facet of In<sub>2</sub>O<sub>3</sub> and the (110) interface facet of the In<sub>2</sub>O<sub>3</sub> crystal structure. From the crystallographic simulation studies, it was evident that the (002) plane possesses only Zn<sup>2+</sup> on the exposed lattice which can facilitate the adsorption of NO<sub>2</sub> molecules and further entrap the electrons and get reduced. Likewise, the (104) and (110) planes of In<sub>2</sub>O<sub>3</sub> terminated with In<sup>3+</sup> ions on the exposed polar planes are also able to grasp the oxygen from the atmosphere and further aid in physical or chemical adsorption of NO<sub>2</sub> molecules.<sup>40</sup> The ZnO (002) plane terminated with Zn<sup>2+</sup> ions and surface anchored In<sub>2</sub>O<sub>3</sub> nanoislands forms the heterojunction structure. The In<sup>3+</sup> terminated planes with the exposed facets of (104) and (110) of In<sub>2</sub>O<sub>3</sub> boost the adsorption kinetics of NO<sub>2</sub> molecules at the heterojunctions. Thus, the crystallographic analysis could predict that the superior adsorption of NO<sub>2</sub> could be mainly caused due to the existence of ZnO/In<sub>2</sub>O<sub>3</sub> polar surfaces by strong dual interactions between Zn<sup>2+</sup> and In<sup>3+</sup> ions on the heterojunctions, which act as a major driving force for the surface reactions during the sensing process.<sup>41</sup> Moreover, the FE-SEM analysis with EDX elemental mapping clearly signified the distribution of Zn, In and O elements on the surface of ZnO as depicted in Fig. 2(i–m), confirming the formation of the ZnO@In<sub>2</sub>O<sub>3</sub> heterojunction nanowires.

TEM analysis (Fig. 2(c) and S3<sup>†</sup>) also revealed the presence of mesoporous structures of the ZnO nanowires which was further correlated and confirmed from N<sub>2</sub> adsorption and desorption studies using BET analysis as depicted in Fig. S3.<sup>†</sup> Both porous and non-porous materials exhibited a characteristic type-IV reversible curve associated with the hysteresis loops at partial pressure ranging from 0.0 to 0.9, representing the presence of a mesoporous structure. The specific surface area, pore volume and pore size of bare ZnO, mesoporous ZnO and mesoporous ZnO@In<sub>2</sub>O<sub>3</sub> heterojunction nanowires were estimated as tabulated in Table S1.<sup>†</sup> The high surface area illustrates the presence of excess active sites on the surface that could aid in easy charge transfer, which can be reflected in superior gas sensing characteristics of the mesoporous ZnO@In<sub>2</sub>O<sub>3</sub> heterojunction nanowires.<sup>20</sup>

### XPS analysis of ZnO@In<sub>2</sub>O<sub>3</sub> heterojunction nanowires

The surface characteristics of ZnO@In<sub>2</sub>O<sub>3</sub> heterojunction nanowires were further examined by XPS analysis. The survey scan spectrum of the ZnO@In<sub>2</sub>O<sub>3</sub> nanowires is depicted in Fig. 3(a). The peaks related to C 1s could originate from the ligands settled during the chemical synthesis and also due to carbon contamination typically found in the survey spectrum. The well-resolved peaks at binding energy values of 1019.8 and 1042.8 eV could be assigned to Zn 2p<sub>3/2</sub> and Zn 2p<sub>1/2</sub> respectively, as shown in Fig. 3(b) whereas, Fig. 3(c) presents the high-resolution In 3d state of ZnO@In<sub>2</sub>O<sub>3</sub> heterojunction nanowires. For In<sub>2</sub>O<sub>3</sub>, a couple of peaks located at 442.9 and 450.5 eV is attributed to the binding energies of In 3d<sub>5/2</sub> and In 3d<sub>3/2</sub>, respectively. Fig. 3(d) shows broad and asymmetric O 1s profiles deconvoluted into



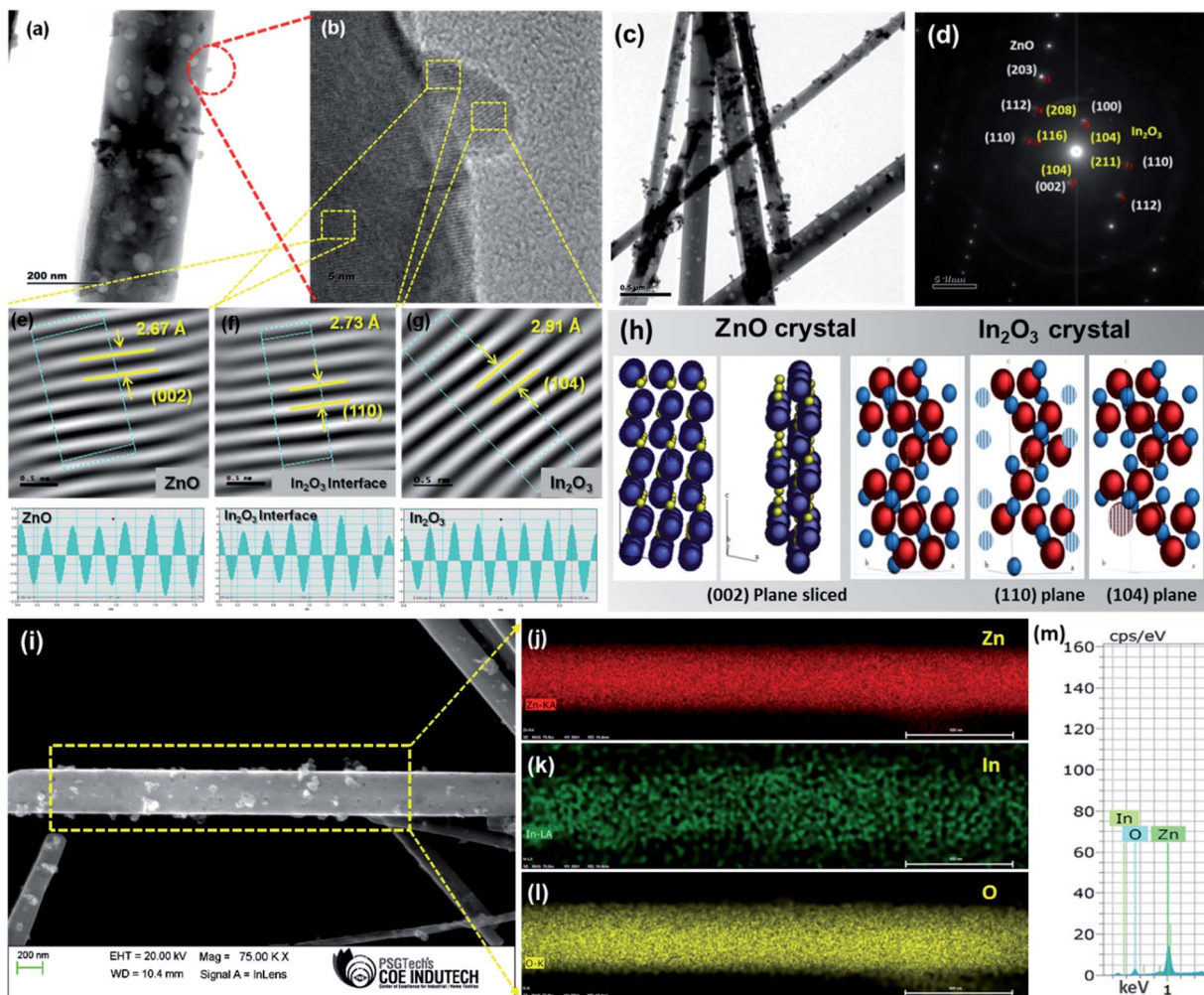


Fig. 2 (a and c) TEM images of  $\text{ZnO}@\text{In}_2\text{O}_3$  heterojunction nanowires, (b) HRTEM image of  $\text{ZnO}@\text{In}_2\text{O}_3$  nanowires, (d) SAED pattern of  $\text{ZnO}@\text{In}_2\text{O}_3$  nanowires, (e–g) the inverse FFT images and estimation of lattice spacing of  $\text{ZnO}$ ,  $\text{In}_2\text{O}_3$  interface and  $\text{In}_2\text{O}_3$  nanoisland planes, (h) simulated crystal planes of  $\text{ZnO}$  and  $\text{In}_2\text{O}_3$ , (i) FE-SEM image of  $\text{ZnO}@\text{In}_2\text{O}_3$  heterojunction nanowires, (j–l) corresponding EDS Elemental maps of  $\text{ZnO}@\text{In}_2\text{O}_3$  heterojunction nanowires and (m) the EDX spectrum shows the presence of Zn, In and O elements.

symmetrical peaks sited at 528.5 and 529.64 eV, respectively indicating a pair of oxygen species ionosorbed on the material. The peak at a binding energy of 528.5 eV is supposed to have originated from the lattice oxide,  $\text{O}^{2-}$  in the  $\text{ZnO}$ , whereas the adjacent peak residing at the binding energy 529.64 eV is ascribed to ionosorbed  $\text{O}^-$  on the surface of  $\text{ZnO}$  nanowires.<sup>42</sup>

#### Room-temperature local current–voltage characteristics of $\text{ZnO}@\text{In}_2\text{O}_3$ heterojunction nanowires

Scanning Spreading Resistance Microscopy (SSRM) imaging was employed to map the local charge transport properties of  $\text{ZnO}@\text{In}_2\text{O}_3$  heterojunction nanowires at room temperature. Fig. 4(a) shows the topography image of n–n type  $\text{ZnO}@\text{In}_2\text{O}_3$  heterojunction nanowires using contact mode AFM imaging. During contact mode SSRM imaging, a bias voltage of  $\pm 5$  V was applied between the conductive tip and the material, as depicted in Fig. 4(b), wherein the resulting current was passed through the tip and sample and was measured in order to

visualize the local spreading resistance. The local electrical conductivity map (Fig. 4(b)) of the n–n type  $\text{ZnO}@\text{In}_2\text{O}_3$  heterojunction nanowires coated on a conductive silicon substrate clearly reveals local electron conduction characteristics across the  $\text{ZnO}@\text{In}_2\text{O}_3$  heterojunction nanowires. The corresponding current–voltage ( $I$ – $V$ ) curves were obtained from various locations on the surface of heterojunction nanowires. The intention of this particular study was to analyze the local electron transport characteristics of the  $\text{ZnO}@\text{In}_2\text{O}_3$  nanowires, in which the conduction in  $\text{ZnO}$  nanowires (27.6 pA) was found to be comparatively higher compared to that in  $\text{In}_2\text{O}_3$  nanoislands (22.3 pA) as evident from Fig. 4(c). It can also be emphasized that the material demonstrated good electrical conductivity at room temperature exclusive of any additional heating to move the electrons within the energy bands. Based on the observation from the SSRM imaging and local current–voltage characteristics of  $\text{ZnO}@\text{In}_2\text{O}_3$  heterojunction nanowires, it can be ascertained that charge accumulation and depletion can occur at the interface of heterojunctions (Scheme 3(b)) as clearly evident



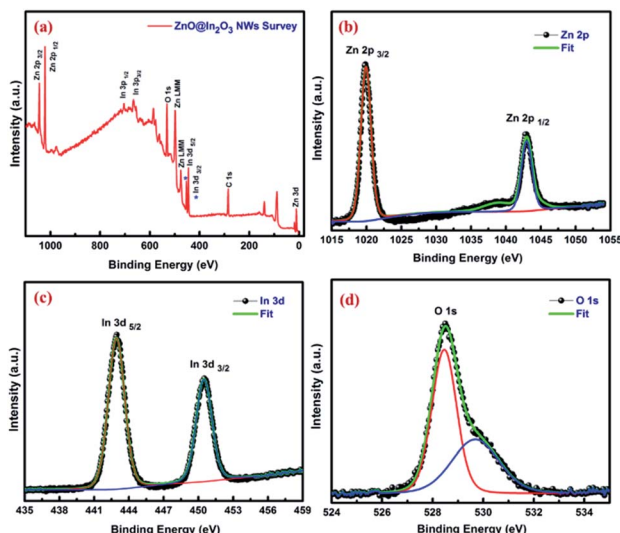


Fig. 3 (a) XPS wide range survey spectrum and high resolution spectra corresponding to (b) Zn 2p (c) In 3d and (d) O 1s of ZnO@In<sub>2</sub>O<sub>3</sub> heterojunction nanowires.

from the color contrast across the nanowires.<sup>43</sup> This can be directly correlated with individual band structures of the semiconducting heterojunctions. While forming the heterojunction, electrons transfer from a lower work function to higher work function material. Hence, the charge transfer occurs from In<sub>2</sub>O<sub>3</sub> to ZnO by which a charge depletion region can be significantly formed at the In<sub>2</sub>O<sub>3</sub> junctions implying the electronic upward bending caused by charge recombination at the interface.<sup>44</sup> In contrast, ZnO (n-type semiconductor) shows higher electron accumulation near to the heterojunction interface, which leads to downward band bending. Therefore, the charge density of ZnO nanowires was found to be higher than that of In<sub>2</sub>O<sub>3</sub> nanoislands, which can lead to remarkably superior NO<sub>2</sub> gas sensing properties owing to the distinctive n-n heterojunction hot spots on the surface of ZnO.

#### Evaluation of the NO<sub>2</sub> sensing performance of ZnO@In<sub>2</sub>O<sub>3</sub> heterojunction nanowires

The NO<sub>2</sub> sensing properties of mesoporous ZnO@In<sub>2</sub>O<sub>3</sub> heterojunction nanowires were evaluated using an in-house gas

sensor test station.<sup>32</sup> In order to estimate the operating temperature, the sensor response ( $S$ ),  $[(R_g - R_a)/R_a]$  upon introduction of 1 ppm of NO<sub>2</sub> gas at different temperatures (RT – 300 °C) was assessed as shown in Fig. 5(a) for porous ZnO nanowires and porous ZnO@In<sub>2</sub>O<sub>3</sub> heterojunction nanowires. The enhanced response toward NO<sub>2</sub> was estimated to be at 150 °C and 34 °C for porous ZnO nanowires and porous ZnO@In<sub>2</sub>O<sub>3</sub> heterojunction nanowires respectively, which were identified as the working temperatures of these sensing materials. The heterojunction nanowires exhibited a significantly reduced working temperature compared to pristine ZnO nanowires. The observed higher response of ZnO@In<sub>2</sub>O<sub>3</sub> heterojunction nanowires under ambient conditions is due to the charge transfer between ZnO and In<sub>2</sub>O<sub>3</sub> due to the difference in work functions. Phenomenally, this process leads to charge accumulation and also the depletion region formed at the interfaces of the heterojunction. Hence, the energy desired to reach the highest response will be minimal for heterojunction ZnO@In<sub>2</sub>O<sub>3</sub> compared to pristine ZnO nanowires which is responsible for its lower operating temperature.

The dynamic NO<sub>2</sub> response characteristics of ZnO nanowires and ZnO@In<sub>2</sub>O<sub>3</sub> heterojunction nanowires towards exposure to various concentrations of NO<sub>2</sub> gas at their optimal operating temperature are depicted in Fig. 5(b and c). The increase in resistance was observed when the material was exposed to NO<sub>2</sub>, which is the typical n-type behavior of a semiconductor and also ascertained with the porous structure of the nanowires. As the gas concentration was increased, the change in resistance was also found to be simultaneously increased. During the sensing property evaluation, the NO<sub>2</sub> gas was introduced along with (N<sub>2</sub>) carrier flow after attaining the stable baseline resistance without any fluctuation. The adsorption of NO<sub>2</sub> gas continued till the saturation was achieved and desorption occurred when NO<sub>2</sub> flow was stopped. The relative response against different concentrations of NO<sub>2</sub> in the range of 500 ppb to 3 ppm was estimated as shown in Fig. 5(d). The NO<sub>2</sub> sensor parameters of ZnO nanowires and ZnO@In<sub>2</sub>O<sub>3</sub> heterojunction nanowires are summarized in Table S2.† The selectivity of the gas sensor is an important parameter for considering them for real time applications. The responses of interfering gases, such as H<sub>2</sub>S, NH<sub>3</sub>, SO<sub>2</sub>, acetone and ethanol were tested at a constant concentration of 2 ppm under ambient conditions. The ZnO@In<sub>2</sub>O<sub>3</sub>

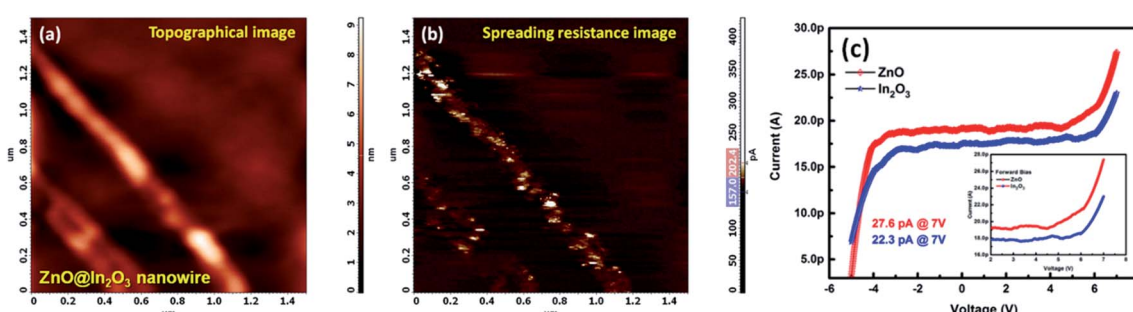


Fig. 4 (a) AFM topography and (b) corresponding SSRM images of ZnO@In<sub>2</sub>O<sub>3</sub> heterojunction nanowires, (c) localized  $I$ – $V$  characteristics of ZnO and In<sub>2</sub>O<sub>3</sub> nanoparticles (inset shows the forward bias  $I$ – $V$  curve).



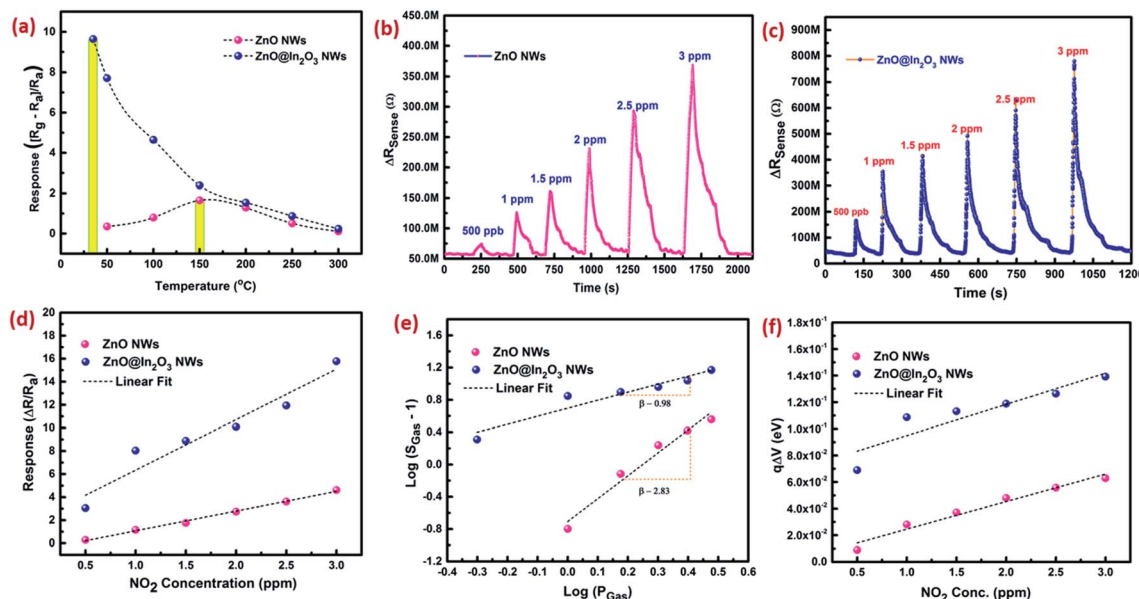


Fig. 5 (a) Response towards exposure to 1 ppm of NO<sub>2</sub> as a function of temperature, (b and c) dynamic NO<sub>2</sub> sensing characteristics, (d) NO<sub>2</sub> response graph, (e) log( $S_{\text{Gas}} - 1$ ) against log  $P_g$  plot of curves and (f) variations in the band bending energy graph of ZnO nanowires and ZnO@In<sub>2</sub>O<sub>3</sub> heterojunction nanowire based sensors.

heterojunction nanowires exhibited good selectivity towards NO<sub>2</sub> gas at room temperature as evident from Fig. S6† compared to other gases. Hence, NO<sub>2</sub> was chosen as the analyte gas for further studies.

Upon exposure of the heterojunction nanowires towards the NO<sub>2</sub> environment, the NO<sub>2</sub> molecules initially react with negatively charged O<sup>2-</sup>, and O<sup>-</sup> ions and seize more electrons from the conduction band rather than interacting directly with the surface. This process reduces the electron accumulation region width ( $L_D$ ) and increases the resistance. Therefore, in order to explore the NO<sub>2</sub> detection mechanism of n-n type ZnO@In<sub>2</sub>O<sub>3</sub> heterojunction nanowires, the state of ionosorbed oxygen molecules has to be initially examined. The sensor response of the material and quantity of the analyte could be correlated with,<sup>45</sup>

$$S_g = \left( \frac{R_g}{R_0} \right) = 1 + (P_g \alpha)^\beta \quad (4)$$

$$\log(S_g - 1) = \beta \log(P_g) + \log \alpha \quad (5)$$

where,  $\alpha$  is the prefactor and  $\beta$  is the typical exponent for partial pressure dependence and  $P_g$  is the analyte concentration. The  $\beta$  value decides the nature of surface oxide species and also elementary reactions that occur on the material surface. If  $\beta$  is equal to 0.5, the surface oxide ions could be O<sup>2-</sup> also if  $\beta$  is  $\sim 1$ , the surface oxide ions could be O<sup>-</sup>. This could be deduced using the relation log( $S_g - 1$ ) against log( $P_g$ ) as shown in Fig. 5(e). As estimated from the slope of the straight line in Fig. 5(e), the  $\beta$  value was calculated to be 2.89 for ZnO nanowires and 1.33 for ZnO@In<sub>2</sub>O<sub>3</sub> heterojunction nanowires at room temperature, signifying that the primary surface oxide species present on ZnO@In<sub>2</sub>O<sub>3</sub> nanowires are O<sub>2</sub><sup>-</sup> rather than O<sup>-</sup> ions.

Moreover, band bending at the heterojunction surface was further estimated based on the sensor response values of ZnO nanowires and ZnO@In<sub>2</sub>O<sub>3</sub> heterojunction nanowires. According to the Boltzmann distribution law, the density of free electrons ( $n_s$ ) and band energy ( $q\Delta V$ ) corresponding to the materials can be related as given below;<sup>46,47</sup>

$$q\Delta V = -K_B \times T \times \ln \left( \frac{R_{\text{air}}}{R_{\text{gas}}} \right) \quad (6)$$

where,  $K_B$  is the Boltzmann constant and  $T$  is the operating temperature.  $R_{\text{gas}}$  is the resistance in a NO<sub>2</sub> atmosphere and  $R_{\text{air}}$  is the resistance in the ambient atmosphere. The band bending can be determined from the sensor response values corresponding to different concentrations of analyte NO<sub>2</sub>. The quantification of  $q\Delta V$  affirmed that ZnO@In<sub>2</sub>O<sub>3</sub> heterojunction nanowires possessed high  $q\Delta V$  energy values compared to pristine ZnO nanowires due to the broader depletion region in the presence of NO<sub>2</sub> as deduced from Fig. 5(f). From this analysis it can be inferred that the existence of ZnO/In<sub>2</sub>O<sub>3</sub> heterojunction interfaces could be responsible for the preferential electron transport and superior NO<sub>2</sub> adsorption process.

To understand the NO<sub>2</sub> adsorption kinetics, the Elovich equation was used and variation of  $(C_{\text{tg}} - C_0)$  versus  $\ln(t)$  was plotted with the help of the response/recovery profiles corresponding to exposure to different concentrations of NO<sub>2</sub> as depicted in Fig. S5(a and b).† As per eqn (S1),† the plot between  $(C_{\text{tg}} - C_0)$  versus  $\ln(t)$  is supposed to be linear.<sup>48,49</sup> Fig. S5(a and b)† illustrate the adsorption isotherms of ZnO nanowires and ZnO@In<sub>2</sub>O<sub>3</sub> heterojunction nanowires, which showed an almost linear trend upon exposure to NO<sub>2</sub> gas. The rate of adsorption can be estimated for different ppm levels of NO<sub>2</sub> which followed a linear trend upon increasing



concentration of  $\text{NO}_2$  (Fig. S5(c)).<sup>†</sup> The initial adsorption rate was calculated to be  $0.93 \Omega^{-1} \text{ s}^{-1}$  at  $150^\circ\text{C}$  for  $\text{ZnO}$  nanowires and  $10.76 \Omega^{-1} \text{ s}^{-1}$  at room temperature for  $\text{ZnO}@\text{In}_2\text{O}_3$  heterojunction nanowires towards 1 ppm of  $\text{NO}_2$  exposure. Further, reduction in the adsorption rate was noticed upon an increase in the  $\text{NO}_2$  concentration owing to continuous cycling of  $\text{NO}_2$ . The effect of concentration on  $\text{NO}_2$  adsorption kinetics was analyzed, which showed an increase in the potential barrier with respect to the  $\text{NO}_2$  concentration. At elevated concentrations, accessibility of  $\text{NO}_2$  molecules was higher on the surface of heterojunction nanowires and therefore, the potential barrier increased as depicted in the Fig. S5(d).<sup>†</sup> The interference of humidity in the  $\text{NO}_2$  sensing performance of  $\text{ZnO}@\text{In}_2\text{O}_3$  heterojunction nanowires was studied as shown in Fig. S7(a and b).<sup>†</sup> The response was found to be relatively constant in the RH (relative humidity) range of 10% to 55%. However, the sensitivity reduced rapidly when the humidity exceeded 60% due to higher RH% interference as moisture adhered on the sensing material restricting the electron transfer between the gas/material interface. The results reveal that  $\text{ZnO}@\text{In}_2\text{O}_3$  heterojunction nanowires have excellent stability at a lower humidity range at room temperature.

### Exploration of a plausible $\text{NO}_2$ sensing mechanism by *in situ* SKPM analysis

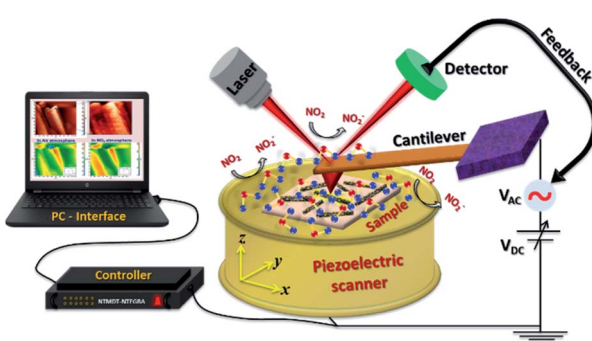
Scanning Kelvin probe microscopy was further implemented to explore the surface potential (SP) variations of the  $\text{ZnO}$  nanowires and n-n type  $\text{ZnO}@\text{In}_2\text{O}_3$  heterojunction nanowires during exposure to the  $\text{NO}_2$  gas environment. By moving the conducting probe towards the material, a biased potential difference is generated owing to the variation in the Fermi energies between the probe and the material.<sup>50</sup> The local charge transport mechanism during  $\text{NO}_2$  gas sensing was further probed by monitoring the surface potential or contact potential difference (CPD) mapping of the n-n type heterojunction nanowires using SKPM during exposure to the  $\text{NO}_2$  gas environment as shown in Scheme 2. The work function, ( $\varphi$ ) of a MOS is defined as the quantity of energy needed to move an electron present in the surface of the semiconductor material to the

vacuum level.<sup>51</sup> A high surface charge density on the material surface therefore promotes higher  $\varphi$ , allowing the visualization of charge accumulation/depletion on the surface of the material. During SKPM analysis, a tungsten carbide coated silicon nitride probe was allowed to interact electronically with the material surface. The contact potential difference (CPD) was measured from the difference between the Fermi levels of the conducting probe and the material surface.<sup>52</sup> The work function of the material ( $\varphi$ ) was determined from the CPD value with the work function of the SKPM cantilever tip,  $\varphi_{(\text{tip})}$ . Before proceeding with SKPM measurements on the heterojunction nanowires, the tungsten carbide coated silicon nitride probe was calibrated on a pure Au thin film under similar conditions (Fig. S4†). The contact potential difference of the Au film was measured to be  $\sim 32$  mV. The work function of the conducting probe ( $\varphi_{(\text{tip})}$ ) was initially calibrated as 4.9 eV estimated using the known work function ( $\varphi_{(\text{Au})} = 5.1$  eV) of the Au sputtered thin film in order to change the calculated CPD into the work function of the material. Moreover, the contact potential difference is extremely material-dependent and directly associated with the work function of the material and surface dipole moments. In the case of semi-conductors, there can be contributions from charge distribution on the material and surface dipoles and from electronic rearrangements at the material/substrate interface. The difference in the work function of the SKPM probe and the material was calculated using the following equations;

$$\text{CPD} = \frac{\Delta\varphi}{e} = \frac{\varphi_{(\text{tip})} - \varphi_{(\text{sample})}}{e} \quad (7)$$

$$e\text{CPD} = \varphi_{(\text{tip})} - \varphi_{(\text{sample})} \quad (8)$$

where  $e$  is the charge,  $\varphi_{(\text{tip})}$  is the work function of the conducting probe and  $\varphi_{(\text{sample})}$  is the work function of the semiconductor material.<sup>53</sup> The topographic AFM images and the corresponding SKPM images of  $\text{ZnO}$  nanowires and  $\text{ZnO}@\text{In}_2\text{O}_3$  heterojunction nanowires before and during  $\text{NO}_2$  exposure are shown in Fig. 6. The CPD before  $\text{NO}_2$  exposure was found to be  $\sim 35$  mV and a two fold increase in CPD upto  $\sim 63$  mV was calculated when  $\text{NO}_2$  was introduced on  $\text{ZnO}$  nanowires. The work function ( $\varphi$ ) of  $\text{ZnO}$  nanowires was estimated to be 4.83 eV before  $\text{NO}_2$  exposure and the work function increased upto 4.93 eV in the  $\text{NO}_2$  environment. Upon exposure to  $\text{NO}_2$  gas, electron transfer occurs between adsorbed  $\text{NO}_2$  and the surface of nanowires which is mainly due to the active oxygen defects and ionosorbed oxide species. The electron depletion leads to increase in CPD which is evident from the SKPM images depicted in Fig. 6(a-c). The morphology and surface potential distribution mapping using SKPM on  $\text{ZnO}@\text{In}_2\text{O}_3$  heterojunction nanowires before and after exposure to the  $\text{NO}_2$  environment are depicted in Fig. 6(d-f). The CPD value of  $\text{ZnO}@\text{In}_2\text{O}_3$  heterojunction nanowires was found to be increased to 103 mV compared to pristine  $\text{ZnO}$  nanowires (35 mV) in the absence of the  $\text{NO}_2$  environment. This enhancement in the CPD value is due to the charge transport between the heterojunction materials



Scheme 2 Schematic representation of *in situ* SKPM imaging performed for  $\text{ZnO}@\text{In}_2\text{O}_3$  heterojunction nanowires in the  $\text{NO}_2$  gas environment.



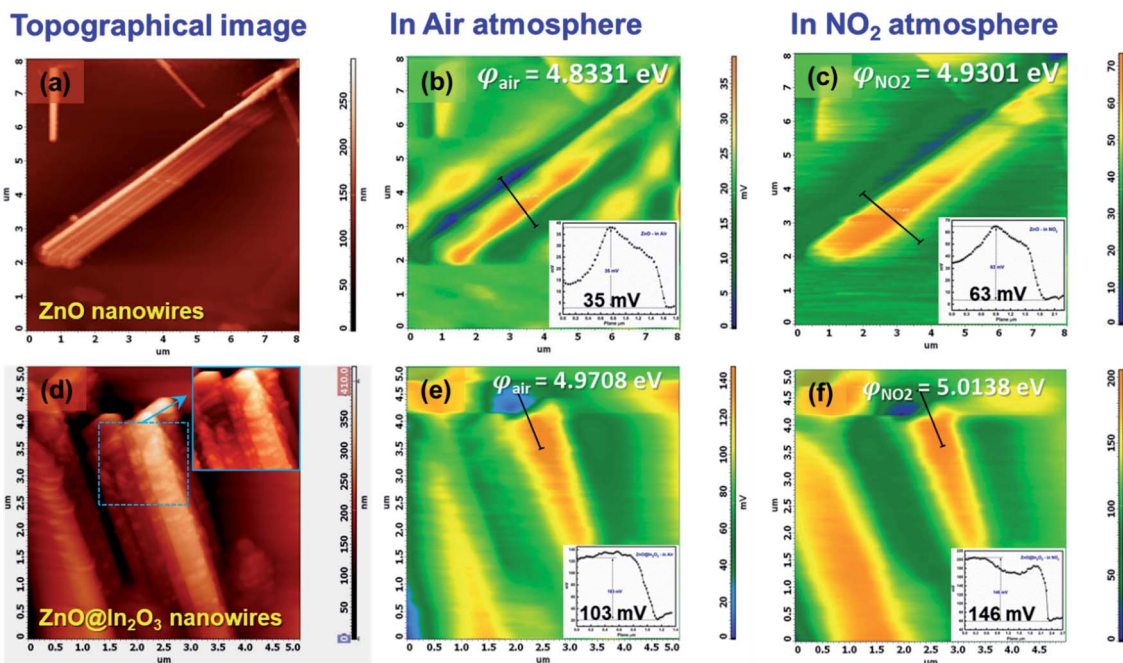


Fig. 6 Representative AFM topographical images of (a) ZnO nanowires and (d) ZnO@In<sub>2</sub>O<sub>3</sub> heterojunction nanowires (inset shows the magnified image of heterojunction nanowires), (b and c) SKPM images of ZnO nanowires in air and the NO<sub>2</sub> environment and (e and f) SKPM images of ZnO@In<sub>2</sub>O<sub>3</sub> heterojunction nanowires in air and NO<sub>2</sub> environments (inset shows the CPD in air and the NO<sub>2</sub> environment).

(In<sub>2</sub>O<sub>3</sub> and ZnO). The electrons in both ZnO nanowires and In<sub>2</sub>O<sub>3</sub> nanoislands acquire different work functions and binding energies when they are electrically connected. Typically, the electrons can move from the material with higher Fermi energy to the material with lower Fermi energy since the work function absolutely depends on the Fermi level. Hence, there could be accumulation of charge and also formation of a depletion region at the heterojunction interfaces. The work function of ZnO@In<sub>2</sub>O<sub>3</sub> heterojunction nanowires was calculated to be 4.97 eV, which is higher than that of bare ZnO nanowires ( $\varphi_{\text{air}} = 4.83$  eV). The increase in the work function indirectly indicates the difference in the Fermi level and surface band bending. The CPD further increased up to 146 mV upon exposure to the NO<sub>2</sub> environment and the corresponding work function was calculated to be 5.02 eV. This enhancement in the CPD value is proportional to the variation in the work function of heterojunction interfaces which can be visualized in the SKPM images as depicted in Fig. 6(d-f). The inset shows the SKPM line scan, denoted by a dark line in Fig. 6(a-c) and (e-f), to measure the CPD before and during NO<sub>2</sub> exposure.

The contact potential difference ( $eV_{\text{CPD}}$ ) between the conducting scanning probe and the material surface corresponds to the variation in their work functions ( $\varphi_{\text{tip}} - \varphi_s$ ).<sup>54</sup> The work function of the semiconductor materials can be estimated using the relations;

$$\varphi_s = -\chi_s + \Phi_B + (E_C - E_F) \quad (9)$$

$$eV_{\text{CPD}} = \varphi_{\text{tip}} - \chi_s + \Phi_B + (E_C - E_F) \quad (10)$$

where,  $e$  is the elementary charge,  $\chi_s$  is the electron affinity of the sample,  $\Phi_B$  is the surface band bending,  $(E_C - E_F)$  is the difference in the Fermi energy ( $E_F$ ) also conduction band ( $E_C$ ) of the material. It is known that the surface potential of the semiconductor materials relies on the surface band bending ( $\Phi_B$ ), the electron affinity ( $\chi_s$ ) and the carrier concentration. The surface band bending (SBB) of ZnO nanowires before and after NO<sub>2</sub> gas exposure using the following equation,

$$\Phi_B = \varphi_M - qV_{\text{CPD}} + \varphi_{\text{off}} - \chi + (E_C - E_F) \quad (11)$$

where,  $\chi$  is the electron affinity of the ZnO (3.2 eV),  $\varphi_{\text{off}}$  is the offset in the estimated work function of the conducting probe found during calibration ( $\sim 32$  meV) on the Au film ( $\varphi_M = 5.1$  eV) and  $E_F$  is the Fermi level related to the conduction band minimum.<sup>28</sup> Using eqn (11), the estimated surface band bending (SBB) of ZnO nanowires before NO<sub>2</sub> exposure was 1.92 eV which was increased upto 1.96 eV during NO<sub>2</sub> exposure. Interestingly, the surface band bending for ZnO@In<sub>2</sub>O<sub>3</sub> heterojunction nanowires was increased up to 2.04 eV compared to pristine ZnO nanowires. During NO<sub>2</sub> exposure, the SBB value increased further up to 2.1 eV which implied the formation of a vast depletion region in the heterojunction nanowires. Based on Boltzmann approximation, the electron density of the ZnO nanowires and ZnO@In<sub>2</sub>O<sub>3</sub> heterojunction nanowires could be estimated, in which the concentration of electrons in n-type semiconductors can be expressed as,

$$n = N_C \exp\left(\frac{E_F - E_C}{K_B T}\right) \quad (12)$$



$$n = N_c \exp \left( \frac{qV_{CPD} - \varphi_{tip} + \chi}{K_B T} \right) \quad (13)$$

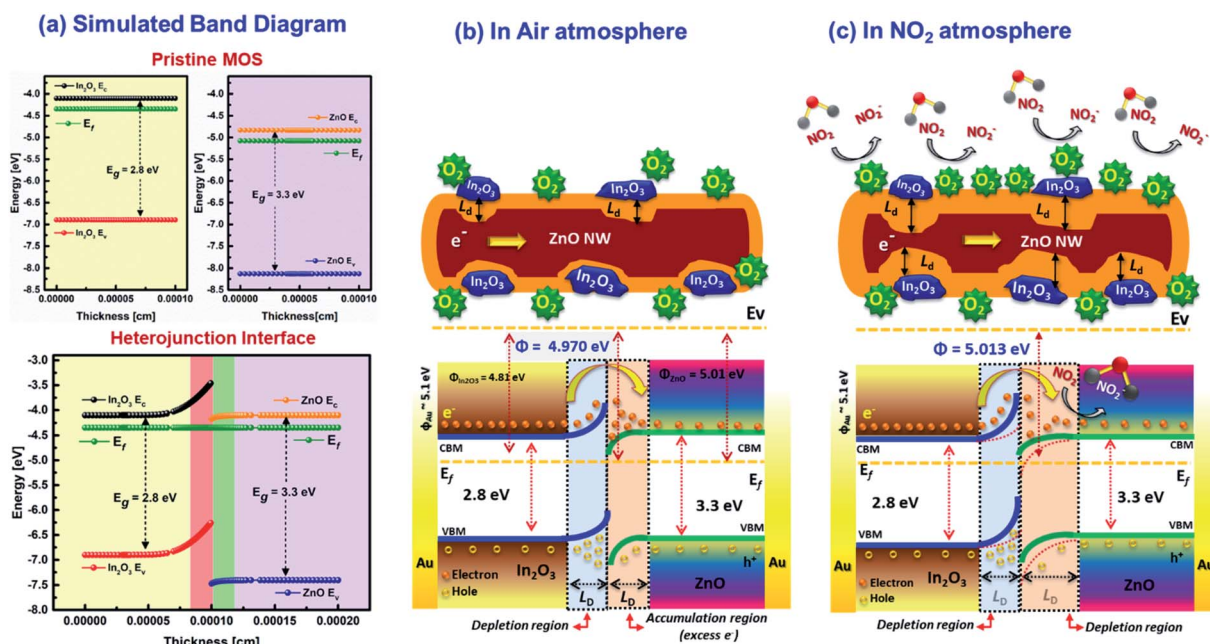
where,  $E_C$  and  $E_F$  are the conduction band and the Fermi energy level,  $N_c$  is the effective density of states,  $T$  is the temperature and  $K_B$  is the Boltzmann constant.<sup>54</sup> Here, the work function of Au was ascertained to be 5.1 eV,  $N_c$  of ZnO is  $3.7 \times 10^{18}$ , electron affinity of ZnO ( $\chi$ ) is 4.5 eV, the Boltzmann constant,  $K_B$  is  $8.6 \times 10^{15}$  eV K<sup>-1</sup> and temperature,  $T$  is 300 K. The carrier density of ZnO nanowires and ZnO@In<sub>2</sub>O<sub>3</sub> heterojunction nanowires before and during NO<sub>2</sub> exposure was calculated from SKPM analysis using eqn (13). The carrier density of ZnO@In<sub>2</sub>O<sub>3</sub> heterojunction nanowires decreased drastically from  $1.18 \times 10^{19}$  cm<sup>-2</sup> to  $0.87 \times 10^{19}$  cm<sup>-2</sup> during NO<sub>2</sub> exposure. The reduction in charge density clearly states that the charge recombination occurs when the NO<sub>2</sub> molecules are adsorbed on ZnO@In<sub>2</sub>O<sub>3</sub> heterojunction nanowires and entrap the electrons present in the conduction band. The space charge region formed due to the SBB at the heterojunction can be described by the depletion width ( $W$ ) and can be expressed as,<sup>28</sup>

$$W = \left( \frac{2\Phi_B \epsilon_0}{q^2 N_D} \right)^{1/2} \quad (14)$$

The depletion width ( $W$ ) formed due to surface band bending and charge carrier density was further calculated from SKPM analysis of ZnO nanowires and ZnO@In<sub>2</sub>O<sub>3</sub> heterojunction nanowires using eqn (14) which is summarized in Table S4.<sup>†</sup> The depletion width ( $W$ ) was found to be increased up to 3.19 nm for heterojunction nanowires compared to pristine ZnO nanowires. During NO<sub>2</sub> exposure, the estimated depletion width was estimated for ZnO nanowires and

ZnO@In<sub>2</sub>O<sub>3</sub> heterojunction nanowires to be 3.34 nm and 3.81 nm respectively. The estimated changes in the work function ( $\varphi_s$ ), depletion width ( $W$ ), surface band bending ( $\Phi_B$ ) and carrier density ( $n_s$ ) values resulting from *in situ* SKPM analysis were further used to deduce the NO<sub>2</sub> sensing mechanism of the ZnO@In<sub>2</sub>O<sub>3</sub> heterojunction nanowires. Based on the above experimental evidence, it can be concluded that the variations in the surface potential of the heterojunction nanowires was increased with decreasing electron density upon NO<sub>2</sub> exposure. The electron-hole pair recombination increases due to the increase in carrier density which favors the charge transport between In<sub>2</sub>O<sub>3</sub> to ZnO at the heterojunctions.

Based on the evidences from SKPM analysis, the electronic band structure was further theoretically constructed using AFORS-HET v2.5 as shown in Scheme 3(a). The simulated energy band diagram clearly revealed the upward bending state at In<sub>2</sub>O<sub>3</sub> and the downward bending state at ZnO interfaces owing to the electron transfer at the heterojunctions due to the difference in their Fermi level energies. The carrier density reaches equilibrium when the Fermi level of the ZnO and In<sub>2</sub>O<sub>3</sub> becomes aligned, while forming heterojunctions. The trapping of electrons at the surface states drastically reduced the surface potential properties. While considering the core-ZnO nanowires, the surface could be occupied by more free electrons than pristine ZnO due to the formation of heterojunctions with In<sub>2</sub>O<sub>3</sub>. This induces a downward bending state and electrons tend to accumulate near the surface of the semiconductor. When electron rich heterojunction nanowires were exposed to NO<sub>2</sub> gas, a majority of carriers tend to be trapped by NO<sub>2</sub> through adsorbed surface oxygen ions (O<sub>2</sub><sup>-</sup>) and the potential barrier of 1D nanowires increased as the carrier density

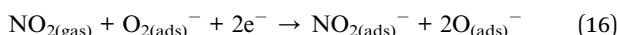


Scheme 3 (a) Simulated energy band diagram before and after contact and schematic diagram showing the NO<sub>2</sub> sensing mechanism (b) in air atmosphere and (c) in the NO<sub>2</sub> gas atmosphere, deduced for ZnO@In<sub>2</sub>O<sub>3</sub> heterojunction nanowires.



decreases resulting in increase in both the SBB and depletion width.

Usually when metal oxide materials are exposed to an oxygen atmosphere, various oxide ions molecules like  $O_2^-$ ,  $O^-$  and  $O^{2-}$  are adsorbed on the material surface as a function of temperature leading to electron depleted regions on the surface of semiconductor materials.<sup>55</sup> At lower working temperatures, more  $O_2^-$  ions can be adsorbed over the surface of ZnO nanowires. The response of the sensor and rate of adsorption of  $NO_2$  molecules may also depend on the surface adsorbed  $O_2^-$  ions. Based on the  $\beta$  value obtained from the  $NO_2$  gas sensing profile, the dominant oxygen species adsorbed over the surface of  $ZnO@In_2O_3$  nanowires were found to be  $O_2^-$  rather than  $O^-$  ions. When the  $ZnO@In_2O_3$  nanowires are exposed to  $NO_2$  gas molecules, the molecules electrically react with negatively adsorbed oxygen molecules and further entrap more electrons at the interfaces of the heterojunction as represented by the given equation:



Based on the experimental evidence and theoretical prediction, the energy diagram of n-ZnO/n-In<sub>2</sub>O<sub>3</sub> heterojunction nanowires is proposed as illustrated in Scheme 3(b and c). The n-n heterojunctions created between n-type ZnO nanowires and n-type In<sub>2</sub>O<sub>3</sub> nanoislands could play a crucial role in tuning the gas sensing performance of the ZnO@In<sub>2</sub>O<sub>3</sub> nanowire based sensor. When In<sub>2</sub>O<sub>3</sub> and ZnO are hybridized to form the n-n type heterojunction, an interfacial electric field could be formed at the interface between ZnO and In<sub>2</sub>O<sub>3</sub>. The energy band-gaps of ZnO and In<sub>2</sub>O<sub>3</sub> were calculated from UV-DRS experiments as 3.31 and 2.75 eV, respectively. Based on these estimated parameters, the simulated band structure designed for n-ZnO and n-In<sub>2</sub>O<sub>3</sub> is shown in Scheme 3(a). The energy band bending state through charge transport, the positions of the conduction and valance bands of n-ZnO/n-In<sub>2</sub>O<sub>3</sub> heterojunctions were clearly understood by simulating the energy band structure using the evidence obtained from the SKPM analysis.

Prior to electrical contact, the Fermi energy of ZnO is lower than that of In<sub>2</sub>O<sub>3</sub> owing to its lower work function illustrated in Scheme S1.† Once these two dissimilar metal oxides with varied work functions are brought into electrical contact, the electrons move out of from higher Fermi energy (In<sub>2</sub>O<sub>3</sub>) to lower Fermi energy (ZnO) until the energy levels achieve equilibrium.<sup>56,57</sup> In the meantime, an interfacial electric charge aligning from core-ZnO to In<sub>2</sub>O<sub>3</sub> is formed at the interfaces. Under air atmosphere (Scheme 3(b)), both In<sub>2</sub>O<sub>3</sub> nanoislands and ZnO nanowires adsorb negatively charged oxygen ions owing to the oxygen adsorption over the sensor material. As a result of the built-in interfacial electric field, the electrons in the conduction band of In<sub>2</sub>O<sub>3</sub> can move to the excited ZnO, and at the same time, holes reside in the valence band of n-In<sub>2</sub>O<sub>3</sub>. Hence, adsorbed oxygen draw electrons from the semiconductor material, making the n-type In<sub>2</sub>O<sub>3</sub> more depleted. This lowered the e-

concentration leads to an upward bending state. Likewise, n-type ZnO become more conductive *i.e.*, an increased e<sup>-</sup> concentration causing a downward bending state. Similarly, when the n-n heterointerface is in contact, the electrons build up near the ZnO/In<sub>2</sub>O<sub>3</sub> junctions forming a depletion region across the In<sub>2</sub>O<sub>3</sub> junctions.<sup>58</sup> During  $NO_2$  exposure which is a strong oxidizing gas, the  $NO_2$  molecules trap e<sup>-</sup> by interaction with  $O_2^-$  ions adsorbed on ZnO and In<sub>2</sub>O<sub>3</sub> interfaces by means of electron transport between the heterojunction interfaces of ZnO@In<sub>2</sub>O<sub>3</sub> nanowires and  $NO_2$  gas molecules as demonstrated in Scheme 3(c). While  $NO_2$  is a potential oxidizing gas with an excessive electron affinity of 2.28 eV in contrast to 0.43 eV of oxygen. The  $NO_2$  gas reacts with the semiconductor heterojunction material *via* ionosorbed  $O_2^-$  species and the potential barrier increases at heterojunction as manifested from *in situ* SSRI and SKPM studies. Furthermore, it was elucidated from the band diagram (Scheme 3(c)) of n-n ZnO@In<sub>2</sub>O<sub>3</sub> heterojunction nanowires that a denser depletion region is formed over the surface of ZnO owing to the electron-hole recombination at the heterojunctions than over In<sub>2</sub>O<sub>3</sub> upon  $NO_2$  exposure as revealed from the experimental evidence stated in the *in situ* SKPM analysis (Fig. 6(f)). Moreover, the crystallographic defects and enhanced surface area owing to the mesoporous structure of the ZnO@In<sub>2</sub>O<sub>3</sub> nanowires provided favourable adsorption facets for a fast response to gaseous  $NO_2$ , which could amplify the gas sensing properties. The gas sensing characteristics of the mesoporous ZnO@In<sub>2</sub>O<sub>3</sub> heterojunction nanowire sensor under ambient conditions are therefore considered to be improved by its distinctive morphological and electrical properties.

## Conclusions

To conclude, 1-D mesoporous n-n type ZnO@In<sub>2</sub>O<sub>3</sub> heterojunction nanowires were effectively synthesized *via* a simple two step hydrothermal method and their local electrical characteristics and  $NO_2$  sensing properties at a reduced operating temperature were thoroughly investigated. Surface-modified In<sub>2</sub>O<sub>3</sub> nanoislands on the ZnO nanowires were characterized by various characterization techniques. XRD and HRTEM analyses illustrated the structure of ZnO@In<sub>2</sub>O<sub>3</sub> heterojunction nanowires as In<sub>2</sub>O<sub>3</sub> nanoislands decorated uniformly over the surface of mesoporous ZnO nanowires. The simulated lattice structure supported by HRTEM analysis was used to presume the  $NO_2$  adsorption on the heterojunction nanowires. The crystallographic analysis was adopted to ascertain the dangling bonds and also estimate the proportion of metals ions to oxygen ions existing at the exposed heterojunction crystal facets. The localized charge transfer process was visualized using spreading resistance imaging, where the maximum electrical conduction occurred at the ZnO sites rather than In<sub>2</sub>O<sub>3</sub> due to the electron transfer between the heterojunctions. The enhanced  $NO_2$  sensing performance of the ZnO@In<sub>2</sub>O<sub>3</sub> sensor is ascribed to the formation of effective n-In<sub>2</sub>O<sub>3</sub>/n-ZnO heterojunctions, resulting in a rapid response time (4–6 s) and 10 times superior sensitivity to ZnO nanowires with a detection limit of 500 ppb of  $NO_2$ . Room temperature *in situ* SKPM



analysis under  $\text{NO}_2$  exposure showed increment in the work function, band bending and depletion width while forming heterojunctions and revealed the local charge transfer processes in heterojunction nanowires pertaining to the  $\text{NO}_2$  sensing process. The boosting of the performance of the sensor was essentially due to Schottky n-n heterojunctions formed at the interfaces of  $\text{ZnO}-\text{In}_2\text{O}_3$  and also due to the increased carrier concentration and rate of oxygen adsorption. This induced the electron depletion layer leading to enhanced  $\text{NO}_2$  gas sensitivity and good selectivity at room temperature. New insights into the sensing mechanism pertaining to n-n type  $\text{ZnO}@\text{In}_2\text{O}_3$  based heterojunction nanowires revealed during this study can be useful for designing novel n-n type MOS heterojunction materials for the development of high performance  $\text{NO}_2$  sensors at a reduced operating temperature for real-time applications.

## Conflicts of interest

There are no conflicts to declare.

## Acknowledgements

The authors would like to acknowledge DST-SERB (SB/S3/CE/038/2015) for financial support. The authors also wish to acknowledge the facilities and support provided by the management, PSG Sons and Charities, Coimbatore.

## Notes and references

- 1 S. Bai, J. Guo, J. Sun, P. Tang, A. Chen, R. Luo and D. Li, *Ind. Eng. Chem. Res.*, 2016, **55**, 5788–5794.
- 2 L. Huang, Z. Wang, J. Zhang, J. Pu, Y. Lin, S. Xu, L. Shen, Q. Chen and W. Shi, *ACS Appl. Mater. Interfaces*, 2014, **6**, 7426–7433.
- 3 J. H. Kim, A. Mirzaei, H. W. Kim and S. S. Kim, *ACS Appl. Mater. Interfaces*, 2019, **11**, 24172–24183.
- 4 X. Chen, S. Wang, C. Su, Y. Han, C. Zou, M. Zeng, N. Hu, Y. Su, Z. Zhou and Z. Yang, *Sens. Actuators, B*, 2020, **305**, 127393.
- 5 Y. Zhong, W. Li, X. Zhao, X. Jiang, S. Lin, Z. Zhen, W. Chen, D. Xie and H. Zhu, *ACS Appl. Mater. Interfaces*, 2019, **11**, 13441–13449.
- 6 Y. Zhang, X. Cheng, X. Zhang, Z. Major, Y. Xu, S. Gao, H. Zhao and L. Huo, *Appl. Surf. Sci.*, 2020, **505**, 144533.
- 7 J. Zhang, D. Zeng, Q. Zhu, J. Wu, Q. Huang and C. Xie, *J. Phys. Chem. C*, 2016, **120**, 3936–3945.
- 8 Z. Wang, G. Men, R. Zhang, F. Gu and D. Han, *Sens. Actuators, B*, 2018, **263**, 218–228.
- 9 F. Eisner, A. Seitkhan, Y. Han, D. Khim, E. Yengel, A. R. Kirmani, J. Xu, F. P. García de Arquer, E. H. Sargent, A. Amassian, Z. Fei, M. Heeney and T. D. Anthopoulos, *Sol. RRL*, 2018, **2**, 1800076.
- 10 B. H. Kim, C. M. Staller, S. H. Cho, S. Heo, C. E. Garrison, J. Kim and D. J. Milliron, *ACS Nano*, 2018, **12**, 3200–3208.
- 11 D. Zhang, J. Wu, P. Li, Y. Cao and Z. Yang, *ACS Appl. Mater. Interfaces*, 2019, **11**, 31245–31256.
- 12 D. Zhang, Z. Yang, Z. Wu and G. Dong, *Sens. Actuators, B*, 2019, **283**, 42–51.
- 13 D. Zhang, Z. Yang, P. Li and X. Zhou, *Sens. Actuators, B*, 2019, **301**, 127081.
- 14 W. Yang, P. Wan, X. Zhou, J. Hu, Y. Guan and L. Feng, *ACS Appl. Mater. Interfaces*, 2014, **6**, 21093–21100.
- 15 S. Bai, H. Fu, Y. Zhao, K. Tian, R. Luo, D. Li and A. Chen, *Sens. Actuators, B*, 2018, **266**, 692–702.
- 16 J. Sun, L. Sun, N. Han, J. Pan, W. Liu, S. Bai, Y. Feng, R. Luo, D. Li and A. Chen, *Sens. Actuators, B*, 2019, **285**, 68–75.
- 17 Y. S. Haiduk, A. A. Khort, N. M. Lapchuk and A. A. Savitsky, *J. SolidState Chem.*, 2019, **273**, 25–31.
- 18 N. Ramgir, R. Bhusari, N. S. Rawat, S. J. Patil, A. K. Debnath, S. C. Gadkari and K. P. Muthe, *Mater. Sci. Semicond. Process.*, 2020, **106**, 104770.
- 19 S. Roso, D. Degler, E. Llobet, N. Barsan and A. Urakawa, *ACS Sens.*, 2017, **2**, 1272–1277.
- 20 K. Zhang, S. Qin, P. Tang, Y. Feng and D. Li, *J. Hazard. Mater.*, 2020, **391**, 122191.
- 21 L. Ma, H. Fan, H. Tian, J. Fang and X. Qian, *Sens. Actuators, B*, 2016, **222**, 508–516.
- 22 K. Xu, S. Tian, J. Zhu, Y. Yang, J. Shi, T. Yu and C. Yuan, *Nanoscale*, 2018, **10**, 20761–20771.
- 23 K. Li, Y. Luo, B. Liu, L. Gao and G. Duan, *J. Mater. Chem. A*, 2019, **7**, 5539–5551.
- 24 P. Hozák, M. Vorokhta, I. Khalakhan, K. Jarkovská, J. Cibulková, P. Fitl, J. Vlček, J. Fara, D. Tomeček, M. Novotný, M. Vorokhta, J. Lančok, I. Matolínová and M. Vrňata, *J. Phys. Chem. C*, 2019, **123**, 29739–29749.
- 25 X. Xiao, L. Liu, J. Ma, Y. Ren, X. Cheng, Y. Zhu, D. Zhao, A. A. Elzatahry, A. Alghamdi and Y. Deng, *ACS Appl. Mater. Interfaces*, 2018, **10**, 1871–1880.
- 26 D. Degler, N. Barz, U. Dettinger, H. Peisert, T. Chassé, U. Weimar and N. Barsan, *Sens. Actuators, B*, 2016, **224**, 256–259.
- 27 C. Drouilly, J. M. Krafft, F. Averseng, S. Casale, D. Bazer-Bachi, C. Chizallet, V. Lecocq, H. Vezin, H. Lauron-Pernot and G. Costentin, *J. Phys. Chem. C*, 2012, **116**, 21297–21307.
- 28 A. Patsha, P. Sahoo, S. Amirthapandian, A. K. Prasad, A. Das, A. K. Tyagi, M. A. Cotta and S. Dhara, *J. Phys. Chem. C*, 2015, **119**, 21251–21260.
- 29 A. Kaur and R. Kumar, *Sens. Actuators, A*, 2016, **245**, 113–118.
- 30 Y. Feng, K. Zhang, H. Li, F. Wang, B. Zhou, M. Fang, W. Wang, J. Wei and H. S. P. Wong, *Nanotechnology*, 2017, **28**, 295705.
- 31 C. E. Kehayas, S. MacNaughton, S. Sonkusale and C. Staii, *Nanotechnology*, 2013, **24**, 245502.
- 32 V. Ramakrishnan, K. G. Nair, J. Dhakshinamoorthy, K. R. Ravi and B. Pullithadathil, *Phys. Chem. Chem. Phys.*, 2020, **22**, 7524–7536.
- 33 V. P. Dinesh, A. Sukhananazerin and P. Biji, *J. Alloys Compd.*, 2017, **712**, 811–821.
- 34 H. Hu, X. Huang, C. Deng, X. Chen and Y. Qian, *Mater. Chem. Phys.*, 2007, **106**, 58–62.
- 35 Y. Wang, S. Li, X. Xing, F. Huang, Y. Shen, A. Xie, X. Wang and J. Zhang, *Chem.-Eur. J.*, 2011, **17**, 4802–4808.



36 F. Liu, G. Huang, X. Wang, X. Xie, G. Xu, G. Lu, X. He, J. Tian and H. Cui, *Sens. Actuators, B*, 2018, **277**, 144–151.

37 R. Zhang, P. G. Yin, N. Wang and L. Guo, *Solid State Sci.*, 2009, **11**, 865–869.

38 S. Sahoo, A. P. S. Gaur, A. K. Arora and R. S. Katiyar, *Chem. Phys. Lett.*, 2011, **510**, 242–245.

39 Y. V. Kaneti, Z. Zhang, J. Yue, Q. M. D. Zakaria, C. Chen, X. Jiang and A. Yu, *Phys. Chem. Chem. Phys.*, 2014, **16**, 11471–11480.

40 S. Bai, L. Quan, P. Tang, Y. Zhao, R. Luo, A. Chen, D. Li and N. Han, *IEEE Sens. J.*, 2016, **16**, 866–872.

41 Z. Xue, Z. Cheng, J. Xu, Q. Xiang, X. Wang and J. Xu, *ACS Appl. Mater. Interfaces*, 2017, **9**, 41559–41567.

42 H. Liu, H. Zhai, C. Hu, J. Yang and Z. Liu, *Nanoscale Res. Lett.*, 2017, **12**, 2–11.

43 M. Kitta and C. Fukada, *Langmuir*, 2019, **35**, 8726–8731.

44 J. Y. Ma, J. Ding, H. J. Yan, D. Wang and J. S. Hu, *ACS Appl. Mater. Interfaces*, 2019, **11**, 21627–21633.

45 J. Dhakshinamoorthy and B. Pullithadathil, *J. Phys. Chem. C*, 2016, **120**, 4087–4096.

46 M. E. Mazhar, G. Faglia, E. Comini, D. Zappa, C. Baratto and G. Sberveglieri, *Sens. Actuators, B*, 2016, **222**, 1257–1263.

47 M. Hübner, C. E. Simion, A. Tomescu-Stănoiu, S. Pokhrel, N. Bârsan and U. Weimar, *Sens. Actuators, B*, 2011, **153**, 347–353.

48 A. V. Raghu, K. K. Karuppanan and B. Pullithadathil, *ACS Sens.*, 2018, **3**, 1811–1821.

49 A. Das, V. Bonu, A. K. Prasad, D. Panda, S. Dhara and A. K. Tyagi, *J. Mater. Chem. C*, 2014, **2**, 164–171.

50 S. R. McKibbin, J. Colvin, A. Troian, J. V. Knutsson, J. L. Webb, G. Otnes, K. Dirscherl, H. Sezen, M. Amati, L. Gregoratti, M. T. Borgström, A. Mikkelsen and R. Timm, *Nano Lett.*, 2020, **20**(2), 887–895.

51 K. Tang, L. Huang, J. Lim, T. Zaveri, J. D. Azoulay and S. Guo, *ACS Appl. Polym. Mater.*, 2019, **11**(1), 2943–2950.

52 R. Pearce, J. Eriksson, T. Iakimov, L. Hultman, A. Lloyd Spetz and R. Yakimova, *ACS Nano*, 2013, **7**, 4647–4656.

53 M. Ali Deeb, J. Ledig, J. Wei, X. Wang, H. H. Wehmann and A. Waag, *J. Appl. Phys.*, 2017, **122**, 085307.

54 Z. Wang, Y. Gu, J. Qi, S. Lu, P. Li, P. Lin and Y. Zhang, *RSC Adv.*, 2015, **5**, 42075–42080.

55 E. Lee, Y. S. Yoon and D. J. Kim, *ACS Sens.*, 2018, **3**, 2045–2060.

56 D. Zhang, Y. Cao, J. Wu and X. Zhang, *Appl. Surf. Sci.*, 2020, **503**, 144063.

57 Z. Yang, D. Zhang and H. Chen, *Sens. Actuators, B*, 2019, **300**, 127037.

58 G. J. Sun, J. K. Lee, S. Choi, W. I. Lee, H. W. Kim and C. Lee, *ACS Appl. Mater. Interfaces*, 2017, **9**, 9975–9985.

